Coupled effects of ocean current on wind stress in the Bay of Bengal: Eddy energetics and upper ocean stratification

Hyodae Seo[a,*], Aneesh C. Subramanian[b], Hajoon Song[c], Jasti S. Chowdary[d]

[a]*Woods Hole Oceanographic Institution, Woods Hole, Massachusetts, USA*

[b]*University of Colorado, Boulder, Colorado, USA*

[c]*Yonsei University, Seoul, Republic of Korea*

[d]*Indian Institute of Tropical Meteorology, Pune, India*

[*]Corresponding author.

E-mail address: hseo@whoi.edu (H. Seo)

ABSTRACT

This study examines the effect of surface current in the bulk formula for the wind stress, referred to as the relative wind (RW) effect, on the energetics of the geostrophic circulation and the upper ocean stratification in the Bay of Bengal (BoB) during the summer monsoon seasons. When the RW effect is taken into account in the high-resolution SCOAR (WRF-ROMS) regional coupled model simulation and compared to the run without such a consideration, the kinetic energy both in the mean (MKE) and eddy (EKE) is reduced by more than a factor of two. The most significant reduction in the kinetic energy is found along the path of the northward East India Coastal Current (EICC) and to the south of its separated latitude. The energetics calculations and spectral analysis reveal that this significant damping of EKE is primarily due to reduced eddy wind work principally at wavelengths close to the first baroclinic Rossby deformation radius, indicating the modulation of the wind work by geostrophic mesoscale eddy fields. Moreover, the mixed layer depth (MLD) is significantly shoaled south of the separated EICC latitude, the area dominated by anticyclonic eddy activity. The shallower mixed layer and enhanced stratification with the RW effect are attributed to doming of the isopycnals by the anomalous upward Ekman

velocity, which itself is generated by the interaction of anticyclonic mesoscale surface current and the prevailing southwesterly monsoonal wind. Overall, the geostrophic circulation and upper ocean stratification along the EICC and south of its separated latitude exhibit the most significant dynamical response. This result implies that this southwestern part of the BoB is a hot spot for the momentum exchange between the surface circulation and the monsoonal winds, thus a potential area for focused field measurements for the ocean circulation energetics and air-sea interaction.

1. Introduction

The mechanical work done by the wind stress on the ocean surface current represents the most significant source of kinetic energy input to the quasi-steady circulation of the oceans (Wunsch, 1998). According to the bulk aerodynamic formula, the wind stress (τ) is calculated as

$$\tau = \rho_a C_D \left(u_a - u_o\right)\left|u_a - u_o\right| \qquad (1),$$

where, ρ_a the density of the air, C_D the drag coefficient, u_a and u_o the wind and ocean surface current velocity, respectively. The term u_a-u_o indicates that the wind stress is determined by the velocity shear across the air-sea interface, not just by the wind. Hereinafter, this will be referred to as the relative wind (RW) effect.

The previous studies have shown that considering the RW effect in the stress formulation produces the wind work that is consistently smaller than the case without consideration of the RW effect. For example, the scaling analysis by Duhaut and Straub (2006) suggests the wind work be reduced by 20% due to the RW effect. More importantly, they showed that the length-scale at which this 20% reduction in the wind work takes place co-occurs with the same length-scale that contains the bulk of oceanic kinetic energy, which implies a linear, scale-to-scale damping effect of the kinetic energy. This damping effect has been espoused by several modeling studies of varying complexity ranging from a quasi-geostrophic ocean model (Hutchinson et al., 2010), ocean general circulation models (Pacanowski, 1987; Zhai and Breatbatch, 2007; Eden and Dietz, 2009; Anderson et al., 2011), coupled general circulation models (Luo et al., 2005) and to more recent high-resolution regional coupled models (Seo et al.,

2007b, 2016; Small et al., 2009; Renault et al., 2016a,b; Seo, 2017). In particular, the results from high-resolution regional coupled models have ascertained that the damping of the ocean kinetic energy by the RW effect, which amounts to 20-50% of the climatology, is particularly efficient over the swift boundary currents, their extensions, and the associated energetic mesoscale eddy fields.

Since the ocean current affects the wind stress, the surface current and the vorticity fields can create changes in Ekman vertical velocities (Thomas and Rhines, 2002; McGillicuddy, 2015). These anomalous Ekman vertical velocities also act to damp the eddy activity by producing Ekman upwelling within the anticyclones (Dewar and Flierl, 1987; Martin and Richards, 2001) and downwelling in the interior of cyclones (Gaube et al., 2015; Seo et al., 2016). Thus, the RW effect is manifested not just in the wind work but also in the Ekman pumping, affecting the oceanic internal instability by displacing the thermocline and the eddy kinetic energy fields.

Recent studies based on satellite observations have also allowed the opportunity to separate this wind-current, or mechanical, coupling effect from the SST-wind thermal coupling effect, the latter of which is shown to be particularly strong at oceanic mesoscale and frontal scales (Chelton 2013; Gaube et al. 2015). Using the high-resolution model simulations, Seo et al. (2016) demonstrated that the dynamical response in the ocean mesoscale fields to these two types of coupling, mechanical and thermal, is highly distinctive. The mechanical coupling consistently works to reduce the energetics of the currents, whereas the thermal coupling, especially at oceanic mesoscale scales, tends to shift the eddy fields (see also Seo 2017). A recent study based on submesoscale resolving coupled model simulations (Renault et al., 2018) further suggested that these two types of coupling are highly scale-dependent, demonstrating that the mechanical coupling is far more effective at the length-scale approaching the oceanic submesoscales.

This study, based on the Bay of Bengal (BoB) during the summer monsoon seasons, attempts to quantify the effect of air-sea coupling on the energetics of the monsoon circulation. We will consider only the mechanical coupling effect in this study, while the thermal coupling is deferred as a future study. However, the BoB, unlike other oceanic boundary currents and their extensions addressed in the previous studies, features a relatively weak expression of the eddy and boundary currents in the SST fields, so we might expect the resulting thermal coupling to be relatively small. Furthermore, it is currently unknown in the literature what the appropriate

satellite-based coupling coefficient might be that relates the crosswind SST gradient and wind stress curl, making it difficult to estimate and validate the SST gradient-induced Ekman pumping velocity from the model simulations. However, knowing the recent evidence that points to the importance of the small-scale SST fronts (e.g. Samanta et al., 2018), all these issues related to thermal coupling remain to be further investigated.

The BoB is an ocean basin surrounded by the landmass to the west, north, and east, so all the water mass exchange with the northern Indian Ocean takes place through the southern open boundary via the seasonally reversing monsoon currents (Schott and McCreary, 2001; Shankar et al., 2002). The summertime (June-September, JJAS) surface circulation in the BoB is characterized by the intense and narrow East India Coastal Current (EICC), which, in summer, flows northward along the southern part of the east coast of India and the southward along the northern part (Shankar et al., 1996; Shankar, 2000; Shetye et al., 1990, 1993; Durand et al., 2009). The northward EICC in the southern part separates from the coast at around 16°N (Potemra et al. 1991; Sil and Chakraborty, 2011; Webber et al., 2018).

The interannual variability and the forcing mechanism of the EICC were investigated by Dadapat et al. (2018) using a numerical model, showing the importance of seasonal coastal Kelvin waves in the development of the EICC. Cheng et al. (2018) examined the eddy statistics and eddy generation mechanisms using satellite observations and a 1-1/2 layer reduced-gravity model to conclude that eddies are mainly generated in the eastern Bay (the tip of the Irrawaddy Delta off Myanmar) by equatorial intraseasonal wind, with nonlinear interaction with coastline geometry and bathymetry. The eddies subsequently propagate southwestward with a period of 30-120 days, and in the western boundary, especially along the EICC path, where the eddy kinetic energy (EKE) reaches the maximum due to enhanced baroclinic and barotropic instabilities that feed the eddy fields (Chen et al., 2018).

A distinguishing feature of the upper ocean structure of the BoB is its strong stratification, with the observed mixed layer depth (MLD) being some of the shallowest in the world oceans (de Boyer Montegut et al., 2007), on the order of 30 m or less, due to the large freshwater flux inputs through local precipitation and river discharges (Seo et al., 2009; Durand et al., 2011; Chowdary et al., 2016). The previous ocean-modeling studies using different wind datasets or artificially increased or decreased strength of the wind forcing, have shown that the skillful simulations of the upper ocean circulation, eddy variability, and the upper ocean stratification in

the ocean general circulation models depends highly on the detailed pattern and strength of the chosen wind forcing (e.g. Dey et al., 2017; Jana et al., 2018). Yet, none of these studies considered the RW effect, which as we will discuss, strongly modulates the wind stress and its curl.

The key results of our study are that the eddy activity is significantly reduced and the MLD significantly shoaled with the consideration of the RW effect. The fact that EKE is reduced may not be surprising. However, the magnitude of the reduction is remarkably large, yielding a factor of two difference in EKE. The shoaling of the MLD is primarily seen over the anticyclonic eddying region in the southwestern basin, where the RW effect generates the upward Ekman velocity, which domes the isopycnals above the thermocline and enhances the near-surface stratification.

2. Model and experiments

2.1. Regional coupled model

This study uses the Scripps Coupled Ocean-Atmosphere Regional (SCOAR) model (Seo et al., 2007a, 2014), which couples the Weather Research and Forecast (WRF; Skamarock et al., 2008) as its atmospheric component with the Regional Ocean Modeling System (ROMS; Haidvogel et al., 2000; Shchepetkin and McWilliams, 2005) as the ocean. The interacting boundary layer is based on the COARE bulk flux algorithm (Fairall et al., 1996, 2003), built in ROMS. The bulk meteorological variables and downward shortwave/longwave radiative fluxes from WRF and the SST and surface current from ROMS are used in the bulk formula to calculate the surface fluxes of heat, momentum, and freshwater every 3 hours. The SCOAR model has been used in a wide range of air-sea studies in the Indian (Seo et al., 2008b, 2009, 2014b; Seo, 2017), the Pacific (Seo et al., 2007a; Putrasahan et al., 2013a,b; Seo et al., 2016) and the Atlantic Oceans (Seo et al., 2006, 2007b, 2008a; 2017; Seo and Xie, 2011).

The model domain covers the BoB north of 10°N (Fig. 1). The horizontal resolutions in WRF and ROMS are identical (5 km) with the matching grids and land-sea mask. The use of identical grids helps to better represent the eddy-forced air-sea flux variability in comparison to a

more typical approach of coupling a coarse atmospheric model to a finer-scale ocean model. The use of identical grids has added benefits of eliminating interpolation errors in the surface fluxes near the coastal boundaries (e.g. Capet et al., 2004; Small et al., 2015) and, without the need for interpolation, improving the numerical efficiency of the coupler (Seo et al., 2009, 2016).

The 5-km resolution in the ocean is designed to better resolve the ocean mesoscale processes and the complex coastlines and estuaries. With the 5 km resolution in the atmosphere, the cumulus convective systems associated with the monsoons can be resolved explicitly. ROMS (WRF) is run with a stretched vertical grid with a total of 50 (35) vertical levels with approximately 15 (10) layers are allotted in the upper 150 m depth (below 750 m height).

Though the WRF model is run without parameterized convection, other processes are still parameterized. The cloud microphysics is represented by the WRF Single-Moment 3-class scheme (Hong et al., 2004) and the planetary boundary layer by the Yonsei University nonlocal scheme (Hong et al., 2006). The Rapid Radiation Transfer Model (RRTM; Mlawer et al., 1997) is used for longwave radiation transfer and the Dudhia broadband SW model (Dudhia, 1989) for the shortwave radiation scheme. The land surface process is treated with the Noah land surface model (Chen and Dudhia, 2001). In ROMS, the Mellor-Yamada level 2.5 turbulence closure scheme (Mellor and Yamada, 1982) with the equilibrium stability function of Kantha and Clayson (1994) determines vertical eddy viscosity and diffusivity. The model does not include mixing parameterizations for the oceanic submesoscales and Langmuir turbulence. No explicit lateral mixing or diffusivity is applied, although the 3rd order upstream biased advection scheme introduces implicit numerical diffusivity (Haidvogel et al., 2000).

At the southern open boundary, the radiation and nudging method is applied to baroclinic components of velocity and tracers (Marchesiello et al., 2001; Di Lorenzo et al., 2003) with the stronger nudging on inflow (time scale of 10 days) than on outflow (120 days). The barotropic components of velocity are treated by Flather (1976) and the free surface by Chapman (1985). Though the eddy dynamics discussed in this study takes places close to the southern boundary, the simulated eddy and circulation features are consistent with several observational estimates and the previous numerical model simulations (Sec. 3a; Jana et al., 2018; Chen et al., 2018; Karmakar et al., 2018). Since the same boundary condition and open boundary treatment are applied to the control and sensitivity experiments and since this study concerns mainly the difference between the two runs, we contemplate that the proximity to the boundary will not

change the interpretation of the results.

In ROMS, the freshwater inputs from the rivers are treated as point sources. The river discharges for the Ganges-Brahmaputra-Meghna (GBM) and the Irrawaddy are obtained from the updated monthly altimeter-based estimates of Papa et al. (2012). The discharge estimates of other rivers, such as the Krishna, Godavari, Mahanadi, Brahmani, Subarnarekha, Hooghly, Sittang, and Salween, are based on monthly climatologies from Jana et al. (2015). The locations of point sources are manually selected based on the proximity of the resolved coastlines to the actual tributaries (Fig. 1; see also Jana, 2015, 2018). The total outflow rate is equally divided into the number of the point sources designated for each of the rivers except for the GBM. For the GBM, 80% of the total outflow is assigned to 15 river mouths east of 90°E, while the rest (20%) to 4 smaller rivers. The discharge is vertically distributed such that 95% of the total transport lies in the top 10 meters. After preliminary sensitivity tests, the salinity of the river waters is set uniformly to 3 psu while the temperature is set to the climatological 2-m air temperatures (Jana et al., 2015). The sensitivity of the BoB circulation to the chosen river salinity values was explored by Jana et al. (2015, 2018), which demonstrated significant improvements in the representation of lifecycle of the freshwater plumes, advection of freshwater, and thus the near-surface stratification with the inclusion of river discharges.

2.2. Experimental setup

Before the WRF-ROMS coupled integrations, the 10-year ROMS spin-up simulation was conducted, with the lateral boundary condition from the climatology of the 5-daily Simple Ocean Data Assimilation (SODA; Carton and Giese, 2008) v3.4.1, which was forced by the ERA-Interim reanalysis (Dee et al., 2011) as the atmospheric forcing. The ROMS spin-up was also forced by the climatological monthly surface fluxes of momentum, heat, and freshwater based on the Comprehensive Ocean-Atmosphere Data Set (da Silva et al., 1994). After the 10-year spin-up, a 10-year hindcast simulation was conducted for 2006-2015 using the monthly ERA-Interim as the atmospheric forcing and the 5-daily SODA v3.4.1 data as the lateral boundary condition.

The ocean state on June 1 from the hindcast simulation was taken as the ROMS initial condition for the SCOAR WRF-ROMS coupled runs. In the coupled run, the 5-daily SODA v3.4.1 data continued to be the boundary condition for ROMS, while the WRF is initialized on

June 1st 00Z and forced at the lateral boundary by the ERA-Interim. The two sets of SCOAR coupled runs were conducted for the summer months (June-September) for 9 years (2007-2015). These two sets of coupled runs differ only in how the wind stress is calculated in the bulk formula in Eq. (1). In CTL, the RW effect is considered in the wind stress calculation, whereas the importance of the RW effect can be diagnosed in an otherwise identical calculation but with the RW omitted (noRW). The difference between CTL and noRW, or the effect of RW, is presented as the percent difference, defined as (CTL-noRW)/CTL*100. The significance of the difference is estimated using a Monte Carlo simulation, randomly scrambled 1000 times, to bootstrap error estimates for the statistical significance at 95%.

The effect of RW on the simulated flow fields can be immediately seen from Fig. 2, which compares the snapshot of the Rossby number (*Ro*, the relative vorticity, ζ, normalized by the local Coriolis frequency, *f*) on June 12, 2009. Since this period is only 12 days after the initialization, the large-scale patterns of *Ro* remain similar, but one can notice that the absolute magnitude of *Ro* in CTL is generally weaker than that of noRW. The probability density function (PDF) of *Ro*, calculated for the entire simulation period (9 summers) and over the whole domain, supports this initial impression. *Ro* in excess of +0.5 is found in both runs; however, CTL shows more regions of smaller *Ro* and fewer areas of intense *Ro*. The superposed black curve denotes the percent difference, confirming that *Ro* is reduced in CTL with the particularly strong reduction in the Ro range of -0.8~-0.5. Therefore, the RW effect in the BoB appears to acts preferentially on the anticyclonic eddies with relatively high *Ro*. The following sections will test this tentative conclusion and investigate in further detail the damping effect of the anticyclonic eddies and its scale dependence.

3. Results

3.1. Changes in mean state

Figure 3 compares the observed and simulated climatologies of the vectors and magnitude of wind stress and surface geostrophic current. The observed wind stress shows the prevailing southwesterly over the Bay with a maximum of 0.1 Nm^{-2} in the interior basin. The

observed geostrophic current estimated from the SODA features the narrow northeastward-flowing EICC in excess of 0.25 ms^{-1}. The northward EICC separates from the coast at 16°N and continues northeastward, while part of the flow recirculates southward anticyclonically, creating large horizontal velocity shear and enhanced eddy activity (Chen et al., 2018). This EICC featured in SODA is qualitatively consistent with other observational estimates such as the OSCAR and AVISO (Jana et al., 2018; Chen et al., 2018). Both CTL and noRW runs overestimate the strength of the observed wind stress. This can be attributed partly to a notable difference in resolution between the ERA-Interim (70 km) and the model (5 km). However, we also note that the ERA-Interim surface wind is already stronger compared to the scatterometer-based estimates of surface wind speed (not shown), implying that the overestimation would also be partly attributed to the pre-existing bias in the ERA-Interim, which is used as the lateral boundary condition. The geostrophic current from the models is more energetic than that inferred from SODA.

There are several notable differences in the climatologies between CTL and noRW, which we interpreted as the cumulative RW effect. The wind stress is reduced in CTL along the EICC but enhanced east and south of it. This difference in wind stress can be easily expected since over the EICC the geostrophic current is in the direction of the prevailing wind, which reduces the wind stress, while the converse is true for south of the EICC where the flow turns anticyclonically. This is the only region within the BoB where the wind stress is increased due to the RW effect, thus experiencing the higher turbulent kinetic energy (Section 3d). The modulation of wind stress by the surface current accounts for 10% of the mean value. In contrast, the difference in wind speed between CTL and noRW is negligible (< 2%, not shown), suggesting that this reduction in wind stress is due to the consideration of the ocean current, not due to change in wind. Outside the region of strong current and eddies, the wind stress is only weakly reduced, and this change is insignificance at the 95% confidence level. The reduced wind stress over the EICC suggests that its circulation in CTL should be less energetic. Indeed, the EICC is substantially weaker in CTL with its maximum speed of 0.3 ms^{-1} in comparison to >0.6 ms^{-1} in noRW. There is also a significant difference in the magnitude of geostrophic current south of the separated EICC latitude.

3.2. Changes in wind work

When the surface stress is modified by the ocean currents, the most direct response should be found in the wind work. The time-mean geostrophic wind work (P_g) is defined following Stern (1975) as

$$P_g = \frac{1}{\rho_0}\left\langle \tau \cdot u_g \right\rangle, \qquad (2)$$

where ρ_0 is the density of the sea water, u_g is the surface geostrophic current vectors, and the angled bracket denotes the time averaging (JJAS averages in each year). u_g can be broken down into the time mean and eddy components, where the eddy component, denoted as primes, is defined as the deviation from the time mean. Here, we ignore the modulation of wind work done on the surface waves (Wang and Huang, 2004) and as well as the Ekman current, which is not expected to produce significant motion within the general circulation (Wunsch, 1998; von Storch et al., 2007; Scott and Xu, 2009). Then P_g becomes

$$P_g = \underbrace{\left\langle \tau \right\rangle \cdot \left\langle u_g \right\rangle}_{P_{gm}} + \underbrace{\left\langle \tau' \cdot u_g' \right\rangle}_{P_{ge}}. \qquad (3)$$

where P_{gm} (P_{ge}) represent the mean (eddy) geostrophic wind work, which will simply refer to as mean (eddy) wind work.

Figure 4 compares the climatology of P_{gm} and P_{ge} between CTL and noRW, along with their zonally integrated meridional profiles. P_{gm} has the maximum positive value along the EICC path, where the geostrophic current is in the direction of the prevailing wind stress. Conversely, P_{gm} is negative to the south since the mean geostrophic current is in the opposite direction of the wind stress. When zonally integrated, P_{gm} is positive north of 12°N with the maximum at 15-16°N and negative south of 12°N. The magnitude of the reduction in the spatially integrated P_{gm} accounts for roughly 39% of the climatology in CTL (Table 1) and is most pronounced in the EICC region (Fig. 4c).

P_{ge} is smaller than P_{gm} by a factor of 5, but it is an important term as it enters the EKE budget directly as either a source or sink. Between CTL and noRW, their absolute magnitudes remain comparable, but the sign switches from positive in noRW to negative in CTL. The negative P_{ge} in CTL means that the geostrophic eddies act as surface drag to the wind stress, thereby serving a sink of the eddy energy. This is in contrast to noRW, where this term is positive, acting as an additional energy source term. As is shown in the next section, this is the

309 area of the EKE maximum and the largest changes in the EKE, implying an active role of
310 mesoscale eddies in the modulation of wind work.
311
312 **3.4. Energetics of geostrophic eddy activity**
313
314 What is the consequence of the reduced geostrophic wind work on the energetics of the
315 general and mesoscale circulation? Figure 5 compares the climatologies of EKE and mean
316 kinetic energy (MKE). For EKE, the altimeter-based estimate is also provided for comparison.
317 The comparison suggests that the model underestimates the high EKEs observed to the south of
318 the separated EICC latitude and along the northwestern coast. This difference stems in part from
319 the bias in the simulated surface circulation in the model as the model underestimates the
320 southwestward branch of the EICC northern BoB (Fig. 3e-f) and thus the associated eddy fields
321 there. Nevertheless, the simulated EKE is in gross agreement with the altimeter-based estimate in
322 terms of magnitude; in both cases, the EKEs exceed 0.1 m^2s^{-2} along the EICC path and its
323 separated latitude. As with the strength of the geostrophic current and wind work, the EKE in
324 noRW is too strong compared to that in CTL; the area-averaged percent difference in EKE
325 climatologies can be nearly 100%. This is also the case with the MKE. The change in MKE
326 would be translated into the EKE through the altered barotropic conversion process in the EKE
327 budget equation (next section).
328 On the one hand, the damping of EKE due to the RW effect is consistent with the finding
329 from a recent study on the Somali Current (Seo, 2017) and other boundary currents and their
330 extensions (Zhai and Breatbatch, 2007; Eden and Dietze, 2007; Seo et al., 2016; Renault et al.,
331 2016a,b). In these boundary current systems, however, the reduction of EKE due to the RW
332 effect is in range of 20-50%, much smaller than what we find in the BoB. We note that the
333 magnitude of the change in wind work due to RW is comparable to the previous studies. This
334 leads to an intriguing question as to why the EKE damping by the RW effect is particularly
335 strong in the BoB given the similar change in wind work. We are not clear about this at this point,
336 although we suspect that it might have to do with the strong salinity stratification in the BoB
337 compared to other basins. This investigation is ongoing and will be reported elsewhere.
338 To quantify the causes of the changes in the EKE, the three diagnostic quantities that
339 represent energy sources and energy conversions are derived from the equations of motion:

340 $$P = P_m + P_e = \frac{1}{\rho_0}\left(\langle u\rangle\langle \tau_x\rangle + \langle v\rangle\langle \tau_y\rangle\right) + \frac{1}{\rho_0}\left(\langle u'\tau_x'\rangle + \langle v'\tau_y'\rangle\right) \quad (4)$$

341 $$BC_{PE\to KE} = -\frac{g}{\rho_0}\int_{-h}^{0}\left(\langle\rho\rangle\langle w\rangle + \langle\rho' w'\rangle\right)dz \quad (5)$$

342 $$BT_{MKE\to EKE} = \int_{-h}^{0} -(\langle u'u'\rangle\frac{\partial U}{\partial x} + \langle u'v'\rangle\frac{\partial U}{\partial y} + \langle v'u'\rangle\frac{\partial V}{\partial x} + \langle v'v'\rangle\frac{\partial V}{\partial y} + \langle u'w'\rangle\frac{\partial U}{\partial z} + \langle v'w'\rangle\frac{\partial V}{\partial z})dz \quad . (6)$$

343 Eq. (4) represents the total work done by the wind stress on the ocean, which can be separated
344 into the mean component (P_m) affecting the MKE and then EKE through barotropic energy
345 conversion, and the eddy wind work (P_e), which enters the EKE budget equation as a source or
346 sink. Eq. (5) denotes the eddy conversion from potential to kinetic energy, particularly important
347 during baroclinic instability (BC). Eq. (6) represents the conversion from MKE to EKE, which is
348 dominated by the horizontal and vertical Reynolds stresses indicative of barotropic instability
349 (BT) and vertical shear instability. We will treat these horizontal and vertical Reynolds stresses
350 as collectively the barotropic process (BT). Given that the kinetic energy decreases significantly
351 below 300 m (Chen et al. 2018), the terms in (4-6) are integrated within prevailing the top 300 m,
352 i.e. h=300m.

353 The results are presented as the climatological differences in each of these terms. The
354 changes in depth-integrated MKE and EKE are similar to those at the surface (Fig. 5), thus not
355 shown. Figure 6 shows P_m, P_e, BT, and BC, in addition to their zonally integrated meridional
356 profiles, color-coded to denote CTL (orange) and noRW (blue). As was discussed before, both
357 the wind work, P_m and P_e, are reduced in CTL (see Table 1), the most pronounced in the western
358 basin. This is also the region of the most energetic eddy activity. The reduced MKE in CTL is
359 translated into the reduced EKE by affecting the shear of the mean and eddy current, and thus the
360 BT, especially between the EICC and the strong eddying region to the south. On the other hand,
361 BC is increased by 11%; the increase in depth-integrated baroclinic energy conversion is unable
362 to explain the reduced EKE in CTL. When zonally integrated, the contribution of changes in BT
363 and BC to the EKE tendency is an order of magnitude smaller than the changes in the eddy wind
364 work, suggesting that the difference in EKE between two runs is a direct result from the
365 difference in the eddy wind work.

366 We also examine the scale-dependence of the changes in energy and its source terms. The
367 top panel of Fig. 7 shows the zonal wavenumber spectra of the surface EKE and EKE tendency

368 and in the bottom the co-spectra between the eddy current and eddy stress and the mean current
369 and mean stress. The spectra were calculated across the zonal width of the Bay (82°-96°E) over
370 the latitudes of 12°-16°N, where the EKE change was the largest, and then the individual spectra
371 were averaged in this latitude band. Also indicated in the right axis of each panel is the percent
372 difference in the spectra, with the negative quantities denoting that the variance is reduced in
373 CTL. We present the co-spectra of current and wind stress instead of the spectra of wind work
374 since the interpretation of the spectrum of a product of two variables can be ambiguous in that
375 the convolution of the spectra of two different variables mixes the signal in spectral space.
376 Nevertheless, we did calculate the spectra of the eddy and mean work to find that the results are
377 in general very similar to those from the co-spectra (not shown).
378 Figure 7a shows that the bulk of the EKE in both CTL and noRW increases toward the
379 lowest wavenumbers. The difference curve, the focus of this analysis, indicates that the EKE
380 variance is reduced nearly by 800% in the wavelengths of approximately 100 km. This length
381 scale corresponds to the first baroclinic Rossby deformation radius in the southwestern BoB
382 (Chelton et al., 1998). A similar result can be seen from the EKE tendency spectra (Fig. 7b). The
383 comparison of the co-spectra of eddy current and stress indicates that the length-scales at which
384 the eddy wind and current contribute most to P_e is also reduced at the similar wavelengths. That
385 the highest declines in EKE and P_e co-occur around the first baroclinic Rossby deformation
386 radius suggests that the reduction of wind work by the RW effect is most effective over the scale
387 of the geostrophic mesoscale eddy fields. The spatial map of the EKE reduction (Fig. 5c)
388 illustrates that this occurs with the geostrophic eddies in the southwestern Bay. The co-spectra of
389 the mean currents and stresses indicate that the variance of P_m in CTL is increased but the
390 percent change is small and shifted toward the longer wavelength than the peak decline in the
391 EKE (we note that the spectrum of P_m shows the decline of the spectral power at this scale).
392
393 *3.4. Upper ocean stratification and Ekman vertical velocity*
394
395 The previous section discussed how the change in geostrophic wind work has led to
396 changes in geostrophic eddy activity. The current section explores the impacts on the upper
397 ocean stratification and MLD. The top panel of Fig. 8 compares the JJAS climatologies of the
398 MLD and the 20°C isothermal layer depth (D20), a proxy for the thermocline depth, along with

399 their differences. MLD is estimated as the depth at which the increase in density from the surface
400 becomes equivalent to the temperature decrease by 0.3°C (the result is relatively insensitive to
401 the choice of criteria). The simulated summer MLD is broadly consistent with the previous
402 estimates based on in situ and Argo data (e.g. Narvekar and Prasanna Kumar, 2014; Prend et al.,
403 2018), showing the deep MLD in the central Bay at 12°-14°N of 30-35 m with the secondary
404 maximum along the western Bay and the gradual northward shoaling following the increasing
405 stratification to the north. However, there are also apparent biases in the simulated MLD
406 compared to other observations-based estimates (e.g. de Boyer Montegut et al., 2007), which
407 may be due to the subjective treatment of river runoff in the model, not to mention the bias in the
408 wind speed (not shown). Between CTL and noRW, the CTL MLD becomes overall shallower in
409 the western and northern basin but deeper in the central basin. However, the changes are mostly
410 insignificant at 95% level except for the region south of the EICC, the area enclosed by the
411 contour of MLD shoaling in CTL by 2 m (black contour in Fig. 8c). There, MLD shoals by up to
412 5 m where the climatological MLD is 20 m. A similar result can be found from the changes in
413 D20, albeit smaller and less significant, which shows the shoaling by up to 10 m where the
414 climatological D20 is about 120 m.
415 What causes the MLD to shoal with the RW effect? Figure 9a-b compares the difference
416 of the Brunt-Väisälä frequency (N^2) and the vertical shear of horizontal current (S^2), both
417 averaged from the surface to D20. The difference is expressed as the percent change. In CTL, N^2
418 is increased by 10% but S^2 decreases by 20-30% in this area. At first sight, the reduced S^2 due to
419 the RW effect is expected given the overall reduced wind stress in the BoB (Fig. 3d). This is,
420 however, with the important exception in the south of the EICC, where the area of increased
421 wind stress due to the RW effect aptly coincides with the bulk of the region where the MLD is
422 reduced. Within the contours of 2 m MLD shoaling in Fig. 9b, in fact, S^2 is less reduced than the
423 ambient areas. This can be confirmed by computing the available turbulent kinetic energy
424 (ATKE) from the surface to D20 as
425 $$ATKE = (\eta_G - \eta_D)\rho v_*^3 - \rho \varepsilon_m h, \qquad (7)$$
426 where v_* denotes the friction velocity, ρ the sea water density, ε_m the background dissipation,
427 taken as $2*10^{-8}$ m^2s^{-3} (Shetye, 1986), and h the D20. The first term on the right-hand side
428 represents the generation of the TKE, and the second term the dissipation. Here, η_G-η_D is treated
429 as constant 1.25 (Kraus and Turner, 1967; Alexander and Kim, 1976; Shetye, 1986; Parekh et al.,

2011). Indeed, the area of increased wind stress and less reduced S^2 marks the enhanced ATKE there. Based on this consideration, the increase in the near-surface turbulence is unable to explain the reduced MLD there.

On the other hand, N^2 increases precisely where MLD is shoaled, so the increase in the upper ocean stratification can be considered as the chief reason for the reduced MLD. To show this, we calculated the energy required for mixing (ERM), following Shenoi et al. (2002) and Agarwal et al. (2012) as

$$ERM = \frac{1}{g}(\rho_b - \rho_s)gh^2, \qquad (8)$$

where ρ_b and ρ_s are the bulk and surface layer density, respectively and h as taken as D20. Physically, ERM represents the difference in potential energy (PE) per unit area before and after mixing (Cushman-Roisin and Beckers, 2012). The PE before mixing is estimated given the simulated stratification in CTL and noRW, while PE after the mixing is estimated assuming the upper ocean has been vertically well mixed. Since ERM represents the upper ocean stratification, the pattern and magnitude of the change in ERM (Fig. 9c) are expected to reflect those of N^2 and the MLD, with the most substantial increase in the region of the maximum MLD shoaling.

The increased N^2 and the shoaled ML with the RW can also be illustrated in Fig. 10 showing the depth-longitude diagrams of the density, N^2, and S^2 over 12-15°N where the anticyclonic eddy fields are dominant. The colored contours denote the lines of constant density, N^2, and S^2 for CTL and noRW, while the differences (CTL-noRW) are shown as the shading. The average MLD and D20 are repeated in each plot. Note that the depth is expressed in the log scale. Within the anticyclonic eddy, the RW effect raises the isopycnals, resulting in higher density anomaly above the thermocline up to 25m just below the MLD. The increase in density between the MLD and D20 is due to reduced temperature and increased salinity in CTL (not shown). As a result of increased density, N^2 is significantly enhanced in CTL below the ML and reduced near the D20 (Fig. 10b). The increased N^2 in the upper isopycnals would hence explain the shallower MLD in CTL. S^2 is significantly reduced in the deeper layer, consistent with the basin-wide reduction in wind work, but near the MLD, there is a hint of increased S^2. Though insignificant, this is congruent with the higher ATKE in this region (Fig. 9d).

Then, why is the N^2 increased with the RW effect in the strong anticyclonic eddying region? We can rule out the role of surface buoyancy or heat fluxes, which only act to damp (not

460 shown). We instead turn our attention to the dissipative effect of the RW on the vorticity
461 dynamics through the eddy-induced Ekman vertical velocity (W). Following Stern (1965) and
462 Gaube et al. (2015), the total wind-driven vertical velocity W (W_{tot}) can be approximately
463 decomposed into the three contributors (without consideration of the SST-induced component),
464 W due to the RW effect (W_c), W due to horizontal vorticity gradient (W_ς), and W due to
465 dependence of zonal wind stress to β (W_β), such that

466 $$W_{tot} = \underbrace{\frac{\nabla \times \tau}{\rho_0 (f+\zeta)}}_{W_c} + \underbrace{\frac{1}{\rho_0 (f+\zeta)^2}\left(\tau_x \frac{\partial \zeta}{\partial y} - \tau_y \frac{\partial \zeta}{\partial x}\right)}_{W_\varsigma} + \underbrace{\frac{\beta \tau_x}{\rho_0 f^2}}_{W_\beta} \quad (9)$$

467 Here, the final term, W_β, is found to be at least an order of magnitude smaller than the first two
468 terms, and thus it is not considered in the subsequent analysis. The percent differences between
469 the first two terms are shown in Fig. 9e-f. In CTL, there is anomalous upward W_c, which is
470 stronger by 100% than that in noRW. The actual amount of increase in the upward W_c is ~10-20
471 cm day^{-1}, i.e. for 120 days per each summer, this anomalous upward motion can alone raise the
472 isopycnals by ~12-24 m. Considering other processes at work, this is broadly consistent with the
473 D20 change shown in Fig. 8f.
474 The percent change in W_ς shows a dipole structure straddling the region of maximum
475 MLD reduction, with a slight upward velocity in the northwest and downward in the southeast.
476 However, the overall change pattern is less coherent, the actual magnitude of increase in W_ς is by
477 order of magnitude smaller than that of W_c, and the change fails to be significant. Therefore, the
478 shoaling of MLD is associated with the doming isopycnals due to anomalous upward Ekman
479 vertical motion brought about by the RW effect. The rise of the thermocline enhances the near-
480 surface stratification (Fig. 10b). In this region, the wind stress and current are in the opposite
481 direction so the increased ATKE can ensue, slightly countering this increased stratification.
482
483 *3.5. Idealized eddy-wind interaction*
484
485 The shoaling of the MLD through the Ekman upwelling velocity is further illustrated in
486 Fig. 11, which depicts realistic and idealized scenarios of sea level anomaly under the
487 southwesterly monsoonal winds. Figure 11a shows the climatologies of sea level anomaly and
488 10-wind vectors in the southwestern BoB from CTL. The mean conditions effectively illustrate

the anticyclonic eddy with a radius (r_0) of ~200 km and an amplitude (A) of 25 cm, as measured based on the difference in sea level between the eddy center (η_c) and the ambient water (η_a). This eddy interacts with the nearly uniform southwesterly surface wind with a speed of 7 ms^{-1}.

This anticyclonic eddy is approximated in an idealized consideration as an axis-symmetric Gaussian eddy, whose sea level anomaly (η) varies as a function of the radial distance,

$$\eta(r) = \eta_a + A\exp\left(-\frac{r^2}{r_0^2}\right), \qquad (10)$$

where we take η_a=50 cm, A=25 cm, and r_0=200 km based on Fig. 11a. This eddy is shown as shading in Fig. 11b. The induced geostrophic surface currents (green vectors) have a maximum speed of 0.27 ms^{-1} at the eddy boundary and turn anticyclonically. The superposed black vectors denote the uniform surface wind of 7 ms^{-1}, reminiscent of the realistic situation depicted in Fig. 11a. Here, for simplicity, we assume there is no SST signature associated with this anticyclonic eddy, although previous studies amply suggest that SST-induced perturbation in wind and wind stress can be substantial (Gaube et al., 2015; Seo et al., 2016; Seo, 2017; Laurindo et al., 2018).

In this scenario, because the surface current is opposite to the wind stress, the RW effect creates the anomalous wind stress that turns cyclonically (black vectors in Fig. 11c). The shading in Fig. 11c denotes W_{tot} calculated from Eq (9), which reveals the upward velocity of up to 0.30 cm day^{-1} northwest of the eddy center and the comparatively weaker downward velocity in the southeast. This W_{tot} results from the combined effect of the two components, W_c and W_ς, as shown separately in Fig. 11d-e. The amplitude and pattern of the perturbation W_c suggest the RW effect alone would create the maximum upward velocity up to 20 cm day^{-1} (or ~24 m per summer) right over the eddy center, consistent with the result from Fig. 9e. The RW effect thus exerts the significant and direct damping effect on the amplitude of the anticyclonic eddy. On the other hand, W_ς features a dipole pattern with the upward velocity in excess of 10 cm day^{-1} in the northwest of the eddy center and downward of the similar magnitude in the southeast, qualitatively consistent with what was shown in Fig. 9f. When W_c and W_ς are combined together, one can expect that, while the spatial pattern of W_{tot} is influenced by W_ς, overall the RW effect is dominant and significantly damps the anticyclonic eddy by doming the isopycnals.

According to McGillicuddy (2015), the RW effect through the eddy-wind interaction can alone transform an anticyclonic eddy into a mode-water eddy through anomalous Ekman vertical velocity. Our study implies that the vertical structure of the isopycnals of the anticyclonic eddy

519 responds similarly, although this is only true in a relative sense. That is, the anticyclonic eddy
520 itself in Fig. 11a is not of a mode-water type, but the process affecting the eddy vertical structure
521 through the RW effect is consistent with the formation mechanism of a mode-water eddy by
522 McGillicuddy (2015). A mode-water eddy was observed in the western Bay of Bengal in winter
523 of 2013 by Gordon et al. (2017), whose formation was also attributed to a result of the
524 interaction of a tropical cyclone with an anticyclonic eddy through air-sea fluxes. Our study
525 suggests that the eddy-wind interaction through the surface current, whether or not the wind is
526 kept spatially uniform as in our idealized case, rotates as considered in an idealized model of
527 McGillicuddy (2015), or is entirely transient as in a fully coupled model, could altogether
528 generate the anomalous upward velocity, doming the isopycnals and enhancing the stratification
529 below the ML. This effect outweighs the enhanced near-surface turbulence, and when combined,
530 the RW effect shoals the MLD over the anticyclonic eddy.
531
532
533 **4. Summary and Discussion**
534
535 This study examines the effect of the inclusion of surface currents, so-called the relative
536 wind (RW) effect, in the bulk formula on the wind work, the Ekman vertical velocities, and the
537 energetics and dynamics of the circulation in the Bay of Bengal (BoB) in summer. Our high-
538 resolution (5 km) SCOAR regional coupled model simulation with explicit convection in the
539 atmosphere captures the RW effect due to the well-resolved surface currents in the ocean (CTL),
540 while an indication of its importance in the overall climatology of the BoB circulation and mixed
541 layer depth (MLD) was identified with an identical twin-experiment where the RW effect is
542 excluded in the bulk formula (noRW).
543 The results show that the energetics of the mean and eddy geostrophic circulation is
544 significantly reduced with the RW effect, improving the realism of the model simulations. This
545 damping effect is most significant south of the separated latitude of the East India Coastal
546 Current (EICC) at 16°N, where the kinetic energy, both the eddy (EKE) and mean (MKE), is
547 reduced in CTL by more than a factor of two. Comparison of the energy source and the depth-
548 integrated barotropic and baroclinic energy conversion processes reveals that the mean
549 geostrophic wind work represents the most significant source of energy for the BoB, which is

reduced by 39% in CTL with the RW effect. The eddy wind work is smaller by a factor of 5 than the geostrophic wind work, but the sign of this term switches from positive (energy source) in noRW to negative (energy sink) in CTL. The eddy wind work enters the EKE budget equation as a source or sink depending on its sign, so this sign change is critical for the EKE reduction in CTL. The mean wind work, on the other hand, translated into the changes in barotropic energy conversion, which, despite achieving as large amplitude as the eddy wind work locally, is still an order of magnitude smaller than the mean wind work when integrated over the Bay. Likewise, the depth-integrated baroclinic conversion processes account for only a small fraction of the EKE tendency and in fact increases in CTL. It is unable to explain the reduced EKE.

Further insights into the changes in the eddy energetics can be gained by comparing the zonal wavenumber spectra of each of these terms. The dramatic decline of the EKE and EKE tendency takes place over wavelengths of around 100 km, the scale of the geostrophic eddy fields that corresponds to the first baroclinic Rossby deformation radius in the southern BoB. These wavelength bands coincide with the wavelengths of the significant reduction of the eddy wind work. Furthermore, there is little difference between the spectra of wind work and the co-spectra of the wind and current. These suggest that the RW effect on wind work and EKE arises from the linear, scale-to-scale coupling between the wind and current.

We also examined the changes in MLD, upper ocean stratification, and Ekman vertical velocities. MLD and, to a lesser extent, thermocline depth (D20), are both shoaled with the RW effect, again most significantly in the southwestern basin of strong anticyclonic eddy activity. Further analysis reveals that, while vertical shear of horizontal currents (S^2) is broadly reduced, the available turbulent kinetic energy (ATKE) is actually increased where the MLD is shoaled. This ATKE increase is because the wind and surface currents are in the opposite direction, which enhances the stress and wind work. Therefore, the increased near-surface turbulence cannot account for the decreased MLD. On the other hand, both the Brunt-Väisälä frequency (N^2) and the energy required for mixing (ERM) are significantly increased in this region of reduced MLD. The vertical sections across the region of strong anticyclonic eddy activity show the increase in density and stratification below the MLD and above the thermocline in CTL.

The question then became what causes the stratification to increase with the RW effect? We suggest that the upward Ekman upward velocity due to RW effect and the induced doming of

581 the isopycnals are mainly responsible. The mechanism is reminiscent of what McGillicuddy
582 (2015) suggested to explain the transformation of an anticyclonic eddy with the positive sea level
583 anomaly into a mode-water type eddy through local eddy-wind interaction. The current-induced
584 Ekman vertical velocity over the anticyclonic eddy is directed upward, doming the isopycnals,
585 and in the process, enhancing the near-surface stratification. On the other hand, the change in
586 Ekman vertical velocity induced by the horizontal vorticity gradient is insignificant, spatially
587 incoherent, and out of phase with the changes in stratification and MLD, and thus its significance
588 to the anomalous doming of the isopycnals in CTL to shoal the MLD could be ruled out.
589
590 Finally, this study demonstrated a rather substantial reduction of the energetics of the ocean
591 currents near the EICC due to the RW effect compared to other ocean boundary currents. In
592 other boundary current systems, the EKE modulation by the RW effect was found in the range of
593 20-50%, compared to 100% as seen in this study. What makes the BoB so sensitive to the RW
594 effect remains unclear, although one could speculate that the strong upper ocean stratification in
595 the BoB, the distinguishing feature from the rest of the ocean basins, could offer a possible
596 answer. One might also suspect the effects of surface gravity waves affecting the wind stress
597 through wave-current interactions (Bye, 1986; Johannessen et al., 1996). Though this process
598 was not considered explicitly in this study, we note that the bulk formula uses the sea-state
599 dependent formulation of the drag coefficient (Fairall et al., 1996; 2003, Edson et al., 2013),
600 which is adopted in the study. The strong monsoon winds over the BoB in the boreal summer
601 support intensified surface wave fields (Shanas and Kumar ,2014; Anoop et al., 2015), whose
602 effect on the air-sea momentum flux could be important for more realistic simulations of the
603 BoB circulation (Jensen et al. 2016). This is a subject of ongoing investigations using idealized
604 ocean-model simulations with different background density stratification and waves effects.
605 Regardless of the mechanisms responsible for the considerable sensitivity of the eddy
606 energetics to the RW effect in the BoB, the results from our experiments imply that to advance
607 our understanding of the upper ocean circulation and the energy pathways, as well as their
608 subsequent coupling with the wind and atmosphere, requires well-resolved, simultaneous
609 measurements of the surface current and wind in the BoB, as well as detailed upper ocean
610 stratification and vertical mixing. This has been the focus of recent several international research
611 activities anchored in the BoB (Wijesekera, et al. 2016; Mahadevan et al., 2016; Vinayachandran

et al., 2018). From these research programs combining the extensive measurements of the upper ocean and meteorological variability with the process-oriented numerical model simulations of various kinds, we expect to advance our understanding of the role of the ocean and air-sea interactions in the monsoon circulations in the ocean and atmosphere and to improve their representation in simulation and prediction models.

Acknowledgments

H. Seo is grateful for support by ONR (N00014-15-1-2588 and N00014-17-1-2398) and NOAA (NA15OAR4310176 and NA17OAR4310255). A. Subramanian acknowledges the support by ONR (N00014-17-S-B001). H. Song is supported by Yonsei University Research Fund (2018-22-0053) and National Research Foundation of Korea (NRF) grant funded by Korea government (MSIST) (NRF-2019R1C1C1003663). J. Chowdary thanks ESSO-IITM and MoES for support. The computing resources were provided by the WHOI High-Performance Computing Facility (https://whoi-it.whoi.edu/resources/). Authors are grateful for river discharge data provided by Dr. Fabrice Papa (LEGOS-IRD). HS also thanks Dr. Sudip Jana (MIT) for his constructive discussions and suggestions, which helped to improve the model simulations and interpretation of the results. Finally, the authors thank the anonymous reviewers for their constructive comments, which helped to substantially improve the manuscript.

References

Agarwal, N., Sharma, R., Parekh, A., Basu, S., Sarkar, A., Agarwal, V., 2012. Argo observations of barrier layer in the tropical Indian Ocean. J. Adv. Space Res. 50, 642–654.

Alexander, R.C., Kim, J.-W., 1976. Diagnostic model study of mixed layer depths in the summer North Pacific. J. Phys. Oceanogr. 6, 293-298.

Anderson, L., McGillicuddy, D., Maltrud, M., Lima, I., Doney, S., 2011. Impact of eddy-wind interaction on eddy demographics and phytoplankton community structure in a model of the north Atlantic ocean. Dyn. Atmos. Oceans. 52, 80–94.

642 Anoop, T.R., Sanil Kumar, V., Shanas, P.R., Johnson, G., 2015. Surface Wave Climatology and
643 Its Variability in the North Indian Ocean Based on ERA-Interim Reanalysis. J. Atmos.
644 Ocean Technol. 32, 1372–1385.
645 Bye, J.A.T., 1986. Momentum exchange at the sea surface by wind stress and understress. Q. J.
646 R. Meteorol. Soc. 112, 501–510.
647 Carton, J.A., Giese, B.S., 2008. A reanalysis of ocean climate using Simple Ocean Data
648 Assimilation (SODA). Mon. Wea. Rev. 136, 2999-3017.
649 Capet, X.J., Marchesiello, P., McWilliams, J.C., 2004. Upwelling response to coastal wind
650 profiles. Geophys. Res. Lett. 31, L13311.
651 Chapman, D.C., 1985. Numerical treatment of cross-shelf open boundaries in a barotropic
652 coastal ocean model. J. Phys. Oceanogr. 15, 1060-1075.
653 Chelton, D.B., deSzoeke, R.A., Schlax, M.G., 1998. Geographical Variability of the First
654 Baroclinic Rossby Radius of Deformation. J. Phys. Oceanogr. 28, 433-460.
655 Chen, F., and Dudhia, J. 2001. Coupling an advanced land surface–hydrology model with the
656 Penn State–NCAR MM5 modeling system. Part I: Model implementation and
657 sensitivity. Mon. Wea. Rev. 129, 569–585.
658 Chen, G., Li, Y., Xie, Q., Wang, D., 2018. Origins of eddy kinetic energy in the Bay of Bengal. J.
659 Geophys. Res. – Oceans 123, 2097–2115.
660 Cheng, X., McCreary, J.P., Qiu, B., Qi, Y., Du, Y., Chen, X., 2018. Dynamics of eddy
661 generation in the central Bay of Bengal. J. Geophys. Res.-Oceans 123, 6861–6875.
662 Chelton, D.B., 2013. Ocean-atmosphere coupling: Mesoscale eddy effects. Nature Geosci. 6,
663 594-595.
664 Kantha, L.H., Clayson, C.A., 1994. An improved mixed layer model for geophysical
665 applications. J. Geophys. Res. 99, 25,235 – 25,266.
666 Cushman-Roisin, B., Beckers, J.-M., 2011. Introduction to Geophysical Fluid Dynamics:
667 Physical and Numerical Aspects, 2nd ed. Academic Press, 425-426 pp.
668 Dandapat, S., Chakraborty, A., Kuttippurath, J., 2018. Interannual variability and characteristics
669 of the East India Coastal Current associated with Indian Ocean Dipole events using a high
670 resolution regional ocean model. Ocean Dynm. 68, 1321-1334.
671 Edson, J., Jampana, V., Weller R., Bigorre, S., Plueddemann, A., Fairall, C., Miller, S., Mahrt, L.,
672 Vickers, D., Hersbach, H., 2013. On the exchange of momentum over the open ocean, J.

673 Phys. Oceanogr. 43, 1589–1610.
674 da Silva, A.M., Young-Molling, C., Levitus, S., 1994. Algorithms and Procedures. Vol. 1, Atlas
675 of Surface Marine Data 1994, NOAA Atlas NESDIS 6, 83 pp.
676 De Boyer Montégut, C., J. Vialard, S.S.C. Shenoi, D. Shankar, F. Durand, C. Ethé and G. Madec,
677 2007. Simulated seasonal and interannual variability of mixed layer heat budget in the
678 northern Indian Ocean. J. Climate 20, 3249-3268.
679 Dee, D., et al., 2011. The ERA-Interim reanalysis: Con- figuration and performance of the data
680 assimilation system. Quart. J. Roy. Meteor. Soc. 137, 553–597.
681 Dewar, W., Flierl, G., 1987. Some effects of the wind on rings. J. Phys. Oceanogr. 17, 1653–
682 1667.
683 Dey, D., Sil, S., Jana, S., Pramanik, S., Pandey, P.C., 2017. An assessment of TropFlux and
684 NCEP air–sea fluxes on ROMS simulations over the Bay of Bengal region. Dyn. Atmos.
685 Oceans 80, 47–61.
686 Di Lorenzo, E., 2003. Seasonal dynamics of the surface circulation in the Southern California
687 Current System. Deep-Sea Res. II 50, 2371-2388.
688 Dudhia, J., 1989. Numerical study of convection observed during the winter monsoon
689 experiment using a mesoscale two-dimensional model. J. Atmos. Sci. 46, 3077–3107.
690 Duhaut, T.H.A., Straub, D.N., 2006. Wind Stress Dependence on Ocean Surface Velocity:
691 Implications for Mechanical Energy Input to Ocean Circulation. J. Phys. Oceanogr. 36, 202–
692 211.
693 Durand, F., Papa, F., Rahman, A., Balam S., 2011. Impact of Ganges–Brahmaputra interannual
694 discharge variations on Bay of Bengal temperature and salinity variations during the 1992–
695 1999 period. J. Earth Syst. Sci. 120, 859–872.
696 Eden, C. and H. Dietze, 2009. Effects of mesoscale eddy/wind interactions on biological new
697 production and eddy kinetic energy. J. Geophys. Res. 114, C05023.
698 Fairall, C., Bradley, E., Godfrey, J., Wick, G., Edson, J. Young, G., 1996. Cool-skin and warm-
699 layer effects on sea surface temperature. J. Geophys. Res. 101, 1295–1308.
700 Fairall, C., Bradley, E.F., Hare, J. Grachev, A., Edson, J., 2003. Bulk parameterization of air-sea
701 fluxes: Updates and verification for the COARE algorithm. J. Climate 16, 571–591.
702 Flather, R.A., 1976. A tidal model of the northwest European continental shelf. "Memoires de la
703 Societe Royale de Sciences de Liege 6, 141-164.

Gaube, P., Chelton, D.B., Samelson, R.M., Schlax, M.G., O'Neill, L.W., 2015. Satellite observations of mesoscale eddy-induced Ekman pumping. J. Phys. Oceanogr. 45, 104-132.

Gordon, A.L., Shroyer, E.L., Mahadevan, A., Sengupta, D., Freilich, M., 2016. Bay of Bengal: 2013 northeast monsoon upper-ocean circulation. Oceanography 29, 82–91.

Haidvogel, D.B., Arango, H.G., Hedstrom, K., Beckmann, A., Malanotte-Rizzoli, P., Shchepetkin, A.F., 2000. Model evaluation experiments in the North Atlantic Basin: Simulations in nonlinear terrain-following coordinates. Dyn. Atmos. Oceans 32, 239–281.

Hong, S.-Y., Dudhia, J., Chen, S.-H., 2004: A revised approach to ice microphysical processes for the bulk parameterization of clouds and precipitation. Mon. Wea. Rev. 132, 103–120.

Hong, S.-Y., Lim, J.-O., 2006. The WRF single-moment 6-class microphysics scheme (WSM6). J. Korean Meteor. Soc. 42, 129-151.

Hutchinson, D.K., Hogg, A.M.C., Blundell, J.R., 2010. Southern ocean response to relative velocity wind stress forcing. J. Phys. Oceanogr. 40, 326–339.

Jana, S., Gangopadhyay, A., Chakraborty, A., 2015. Impact of seasonal river input on the Bay of Bengal simulation. Cont. Shelf Res. 104, 45–62.

Jana, S., Gangopadhyay, A., Lermusiaux, P.F.J., Chakraborty, A., Sil, S., Haley Jr., P.J., 2018. Sensitivity of the Bay of Bengal upper ocean to different winds and river input conditions. J. Mar. Syst. 187, 206-222.

Jensen, T.G., Wijesekera, H.W., Nyadjro, E.S., Thoppil, P.G., Shriver, J.F., Sandeep, K.K., Pant, V., 2016. Modeling salinity exchanges between the equatorial Indian Ocean and the Bay of Bengal. Oceanography 29, 92–101.

Karmakar, A, Parekh, A., Chowdary, J.S., Gnanaseelan, C., 2018. Inter comparison of Tropical Indian Ocean features in different ocean reanalysis products. Clim. Dynm. 51, 119-141.

Kraus, E., Turner, J., 1967. A one dimensional model of the seasonal thermocline II: The general theory and its consequences. Tellus 19, 98–106.

Laurindo, L.C., Siqueira, L., Mariano, A.J., Kirtman, B., 2018. Cross-spectral analysis of the SST/10-m wind speedcoupling resolved by satellite products and climate model simulations. Clim. Dyn. 52, 5071-5098.

Luo, J-J., Masson, S., Roeckner, E., Madec, G., Yamagata, T., 2005. Reducing Climatology Bias in an Ocean-Atmosphere CGCM with Improved Coupling Physics. J. Climate 18, 2344-2360.

Marchesiello, P., McWilliams, J.C., Shchepetkin, A., 2003. Equilibrium structure and dynamics

735 of the California Current System. J. Phys. Oceanogr. 33, 753–783,
736 McGillicuddy, D.J., 2015. Formation of Intrathermocline Lenses by Eddy–Wind Interaction. J.
737 Phys. Oceanogr. 45, 606–612.
738 Mahadevan, A., Paluszkiewicz, T., Ravichandran, M., Sengupta, D., Tandon, A., 2016.
739 Introduction to the special issue on the Bay of Bengal: From monsoons to mixing.
740 Oceanography 29, 14–17.
741 Mellor, G.D., Yamada, T., 1982. Development of a turbulence closure model for geophysical
742 fluid problems. Rev. Geophys. 20, 851-875.
743 Mlawer, E.J., Taubman, S.J., Brown, P.D., Iacono, Clough, S.A., 1997. Radiative transfer for
744 inhomogeneous atmospheres: RRTM, a validated correlated-k model for the longwave. J.
745 Geophys. Res. 102, 16663-16682.
746 Narvekar, J., Prasanna Kumar, S., 2014. Mixed layer variability and chlorophyll a biomass in the
747 Bay of Bengal. Biogeosciences 11, 3819-3843.
748 Pacanowski, R. C., 1987. Effect of Equatorial Currents on Surface Stress. J. Phys. Oceanogr. 17,
749 833-838.
750 Papa, F., Bala, S.K., Pandey, R.K., Durand, F., Gopalakrishna, V.V., Rahman, A., Rossow, W.B.,
751 2012. Ganga- Brahmaputra river discharge from Jason-2 radar altimetry: An update to the
752 long-term satellite-derived estimates of continental freshwater forcing flux into the Bay of
753 Bengal, J. Geophys. Res. 117, C11021.
754 Parekh, A., Gnanaseelan, C., Jayakumar, A., 2011. Impact of improved momentum transfer
755 coefficients on the dynamics and thermodynamics of the north Indian Ocean. J. Geophys.
756 Res. 116, C01004.
757 Potemra, J.T., Luther, M.E., O'Brien, J.J., 1991. The seasonal circulation of the upper ocean in
758 the Bay of Bengal. J. Geophys. Res. 96, 12,667-12,683.
759 Putrasahan, D., Miller, A.J., Seo, H., 2013a. Isolating Mesoscale Coupled Ocean-Atmosphere
760 Interactions in the Kuroshio Extension Region. Dyn. Atmos. Oceans 63, 60-78.
761 Putrasahan, D., Miller, A.J., Seo, H., 2013b. Regional coupled ocean-atmosphere downscaling in
762 the Southeast Pacific: Impacts on upwelling, mesoscale air-sea fluxes, and ocean eddies.
763 Ocean Dynam. 63, 463-488.
764 Prasad, T.G., 2004. A comparison of mixed-layer dynamics between the Arabian Sea and Bay of
765 Bengal: One- dimensional model results, J. Geophys. Res. 109, C03035.

766 Prend, C. J., Seo, H., Weller, R.A., Farrar, J.T., 2018. Impact of freshwater plumes on
767 intraseasonal upper ocean variability in the Bay of Bengal. Deep-Sea Res.-II 161, 63-81.
768 Renault, L., Molemaker, M.J., McWilliams, J.C., Shchepetkin, A.F., Lemaré, F., Chelton, D.,
769 Illig, S., Hall, A., 2016a. Modulation of wind work by oceanic current interaction with the
770 atmosphere. J. Phys. Oceanogr. 46, 1685–1704.
771 Renault, L., Molemaker, M.J., Gula, J., Masson, S., McWilliams, J.C., 2016b. Control and
772 Stabilization of the Gulf Stream by Oceanic Current Interaction with the Atmosphere. J.
773 Climate 46, 3439-3453.
774 Renault, L., McWilliams, J.C., Gula, J., 2018. Dampening of submesoscale currents by air-sea
775 stress coupling in the californian upwelling system. Scientific Reports 8, 13388.
776 Samanta, D., Saji, H.N., Jin, D., Thilakan, V., Ganai, M., Rao, S.A., Deshpande, M., 2018.
777 Impact of a Narrow Coastal Bay of Bengal Sea Surface Temperature Front on an Indian
778 Summer Monsoon Simulation. Scientific Reports 8, 17694.
779 Schott, F.A., McCreary, J.P., 2001. The monsoon circulation of the Indian Ocean. Prog.
780 Oceanogr. 51, 1–123.
781 Seo, H., Jochum, M., Murtugudde, R., Miller, A. J., 2006. Effect of Ocean Mesoscale Variability
782 on the Mean State of Tropical Atlantic Climate. Geoyphs. Res. Lett. 33, L09606.
783 Seo, H., Miller, A.J., Roads, J.O., 2007a. The Scripps Coupled Ocean-Atmosphere Regional
784 (SCOAR) model, with applications in the eastern Pacific sector. J. Climate 20, 381-402.
785 Seo, H., Jochum, M., Murtugudde, R., Miller, A.J., Roads, J.O., 2007b. Feedback of Tropical
786 Instability Wave - induced Atmospheric Variability onto the Ocean. J. Climate 20, 5842-
787 5855.
788 Seo, H., Jochum, M., Murtugudde, R., Miller, A.J. Roads, J.O., 2008a. Precipitation from
789 African Easterly Waves in a Coupled Model of the Tropical Atlantic. J. Climate 21, 1417-
790 1431.
791 Seo, H., Murtugudde, R., Jochum, M., Miller, A.J., 2008b. Modeling of Mesoscale Coupled
792 Ocean-Atmosphere Interaction and its Feedback to Ocean in the Western Arabian Sea. Ocean
793 Modell. 25, 120-131.
794 Seo, H., Xie, S.-P., Murtugudde, R., Jochum, M., Miller, A.J., 2009. Seasonal effects of Indian
795 Ocean freshwater forcing in a regional coupled model. J. Climate 22, 6577-6596.

796 Seo, H., Xie, S.-P., 2011. Response and Impact of Equatorial Ocean Dynamics and Tropical
797 Instability Waves in the Tropical Atlantic under Global Warming: A regional coupled
798 downscaling study. J. Geophys. Res.-Oceans 116, C03026.
799 Seo, H., Xie, S.-P., 2013. Impact of ocean warm layer thickness on the intensity of hurricane
800 Katrina in a regional coupled model. Meteor. Atmos. Phys. 122, 19-32.
801 Seo, H., Subramanian, A.C., Miller, A.J., Cavanaugh, N.R., 2014. Coupled impacts of the
802 diurnal cycle of sea surface temperature on the Madden-Julian Oscillation. J. Climate 27,
803 8422-8443.
804 Seo, H., Miller, A.J. Norris, J.R., 2016. Eddy-wind interaction in the California Current System:
805 dynamics and impacts, J. Phys. Oceanogr., 46, 439-459
806 Seo, H., 2017: Distinct influence of air-sea interactions mediated by mesoscale sea surface
807 temperature and surface current in the Arabian Sea. J. Climate 30, 8061-8079
808 Shanas, P.R., Kumar, V.S., 2014. Temporal variations in the wind and wave climate at a location
809 in the eastern Arabian Sea based on ERA-Interim reanalysis data. Nat. Hazards Earth Syst.
810 Sci. 14, 1371–1381
811 Shankar, D., McCreary, J.P., Han, W., Shetye, S.R., 1996. Dynamics of the East India Coastal
812 Current: 1. Analytic solutions forced by interior Ekman pumping and local alongshore winds.
813 J. Geophys. Res. 101, 13975–13991.
814 Shankar, D., 2000. Seasonal cycle of sea level and currents along the coast of India. Current
815 Science 78, 279–288.
816 Shankar, D., Vinayachandran, P.N., Unnikrishnan, A.S., Shetye, S.R., 2002. The monsoon
817 currents in the north Indian Ocean. Prog. Oceanogr. 52, 63–120.
818 Shchepetkin, A.F., McWilliams, J.C., 2005. The regional oceanic modeling system (ROMS): a
819 split-explicit, free-surface, topography-following-coordinate ocean model. Ocean Modell. 9,
820 347-404.
821 Shenoi, S.S.C., Shankar, D., Shetye, S.R., 2002. Differences in heat budgets of the near-surface
822 Arabian Sea and Bay of Bengal: Implications for the summer monsoon. J. Geophys. Res. 107,
823 3052.
824 Shetye, S.R., 1986. A model study of the seasonal cycle of the Arabian Sea surface temperature.
825 J. Mar. Res., 44, 521–542.

826 Shetye, S.R., Gouveia, A.D., Shenoi, S.S.C., Sundar, D., Michael, G.S., Almeida, A.M.,
827 Santanam, K,. 1990. Hydrography and circulation off the west coast of India during the
828 southwest monsoon 1987. J. Mar. Res. 48, 359–378.
829 Shetye, S.R., Gouveia, A.D., Shenoi, S.S.C., Sundar, D., Michael, G.S., Nampoothiri, G., 1993.
830 The western boundary current of the seasonal subtropical gyre in the Bay of Bengal. J.
831 Geophys. Res. 98, 945–954.
832 Sil, S., Chakraborty, A., 2011. Simulation of east India coastal features and validation with
833 satellite altimetry and drifter climatology. Int. J. Oceans Clim. Syst. 2, 279–289.
834 Skamarock, W.C., Klemp, J.B., Dudhia, J., Gill, D.O., Barker, D.M., Duda, M.G., Huang, X.,
835 Wang, W., Powers, J.G., 2008. A description of the advanced research WRF version 3. Rep.
836 NCAR/TN-475+STR, Natl. Cent. for Atmos. Res., Boulder, Colo.
837 Small, R.J., Richards, K.J., Xie, S.-P., Dutrieux, P., Miyama, T., 2009. Damping of Tropical
838 Instability Waves caused by the action of surface currents on stress. J. Geophys. Res. 114,
839 C04009.
840 Small, R.J., Curchistern, E., Hedstrom, K., Kauffman, B., Large, W., 2015. The Benguela
841 upwelling system: Quantifying the sensitivity to resolution and coastal wind representation in
842 a global climate model. J. Climate 28, 9409-9432.
843 Stern, M., 1965. Interaction of a uniform wind stress with a geostrophic vortex. Deep Sea
844 Research and Oceanographic Abstracts 12, 355–367.
845 Stern, M.E., 1975. Ocean Circulation Physics. Academic Press, 275 pp.
846 Thomas, L.N., Rhines, P.R., 2002. Nonlinear stratified spin-up. J. Fluid. Mech. 473, 211-244.
847 Von Storch, J.-S., Sasaki, H., Marotzke, J., 2007: Wind-Generated Power Input to the Deep
848 Ocean: An Estimate Using a 1/10° General Circulation Model. J. Geophys. Oceanogr. 37,
849 657- 672.
850 Wang, W., Huang, R.X., 2004: Wind Energy Input to the Ekman Layer. J. Phys. Oceanogr. 34,
851 1267-1275.
852 Webber, B.G.M., Matthews, A.J., Vinayachandran, P.N., Neema, C.P., Sanchez-Franks, A.,
853 Vijith, V., Amol, P., Baranowski, D.B., 2018. The dynamics of the Southwest Monsoon
854 current in 2016 from high-resolution in situ observations and models. J. Phys. Oceanogr. 48,
855 2259-2282.

Wijesekera, H.W., Teague, W.J., Wang, D.W., Jarosz, E., Jensen, T.G., Jinadasa, S.U.P., Fernando, H.J.S., Hallock, Z.R., 2016: Low-frequency currents from deep moorings in the southern Bay of Bengal. J. Phys. Oceanogr. 46, 3209–3238.

Wunsch, C., 1998: The work done by the wind on the oceanic general circulation. J. Phys. Oceanogr. 28, 2332–2340.

Zhai, X., Greatbatch, R.J., 2007: Wind work in a model of the northwest Atlantic ocean. Geophys. Res. Lett. 34, L04606.

Table 1: The spatially integrated energy source and depth-integrated energy conversion terms (10^5 m^5s^{-3}). The percent difference is defined as (CTL- noRW)/CTL *100, with the negative values denoting the decrease in CTL.

	P_{gm}	P_e	BT	BC
CTL	25.1	-5.03	4.51	13.9
noRW	34.9	7.48	7.36	12.3
% difference	-39%	-249%	-63%	+12%

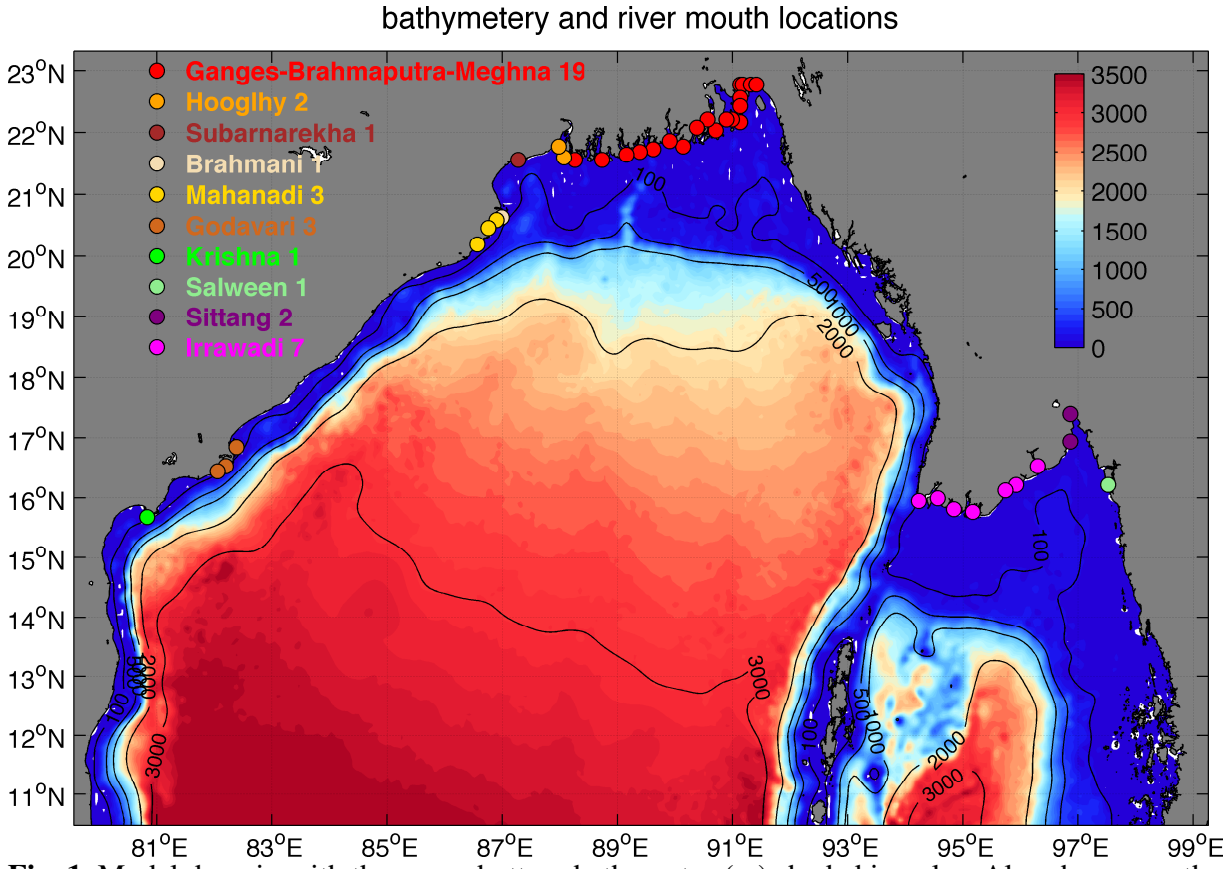

Fig. 1. Model domain with the ocean bottom bathymetry (m) shaded in color. Also shown are the locations and number of the point sources of the river discharges, color-coded to represent each of the rivers.

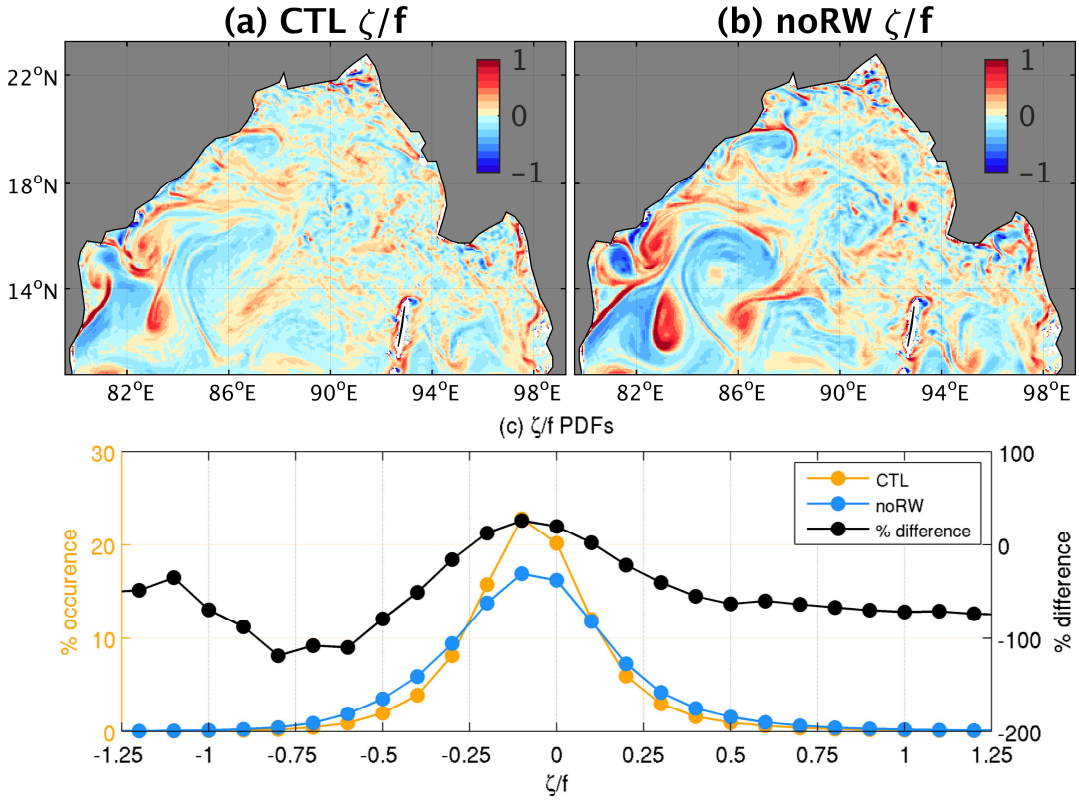

Fig. 2. Snapshots of relative vorticity normalized by local Coriolis frequency (*ζ/f*) on June 12, 2009 from (a) CTL and (b) noRW. (c) Histograms of ζ/f over the whole domain for the summers of 2007-2015 and their percent difference.

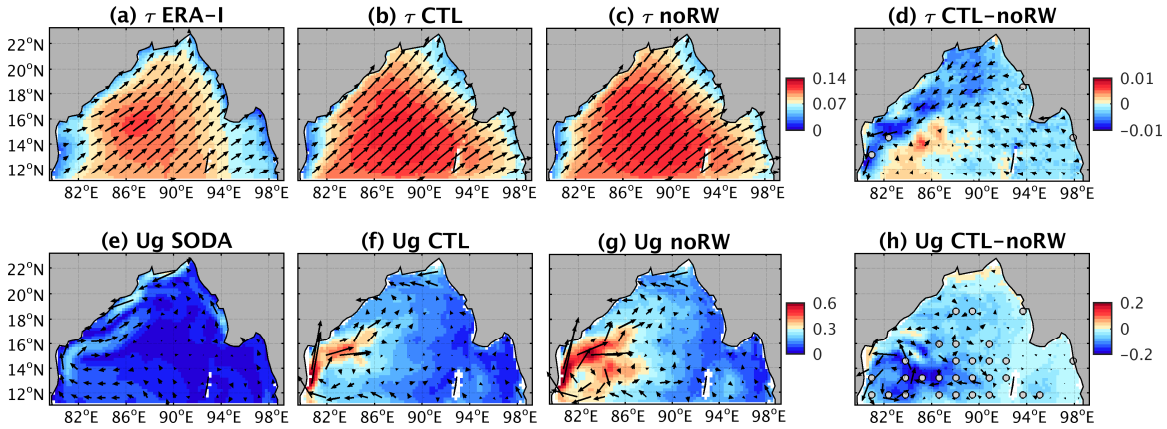

Fig. 3. The JJAS climatologies of (top) wind stress vectors and magnitude (Nm^{-2}) and (bottom) geostrophic surface current (ms^{-1}) from (left to right) observations, CTL and noRW. Dots denote the areas of significant difference at 95% confidence level, evaluated with the confidence interval obtained by a Monte Carlo bootstrap sampling (1000 times).

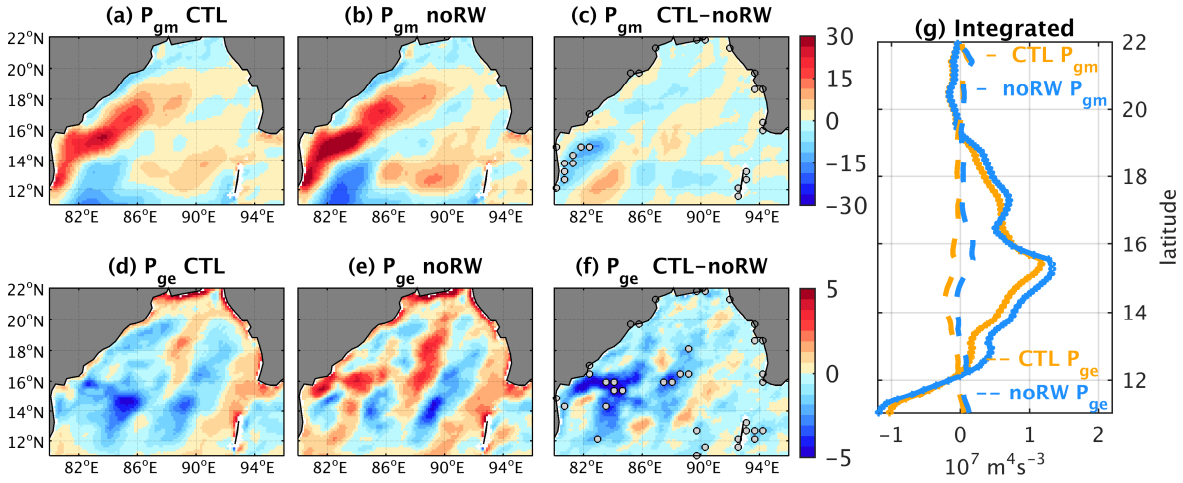

Fig. 4. Mean geostrophic wind work (P_{gm}, 10^6 m^3s^{-3}) from (a) CTL and (b) noRW, and (c) the difference. (d-f) as in (a-c) except for time-mean eddy geostrophic wind work (P_{ge}). Dots representing the statistical significance at 95% confidence level. (g) Zonally integrated P_{gm} and P_{ge} (m^4s^{-3}) as a function of latitude.

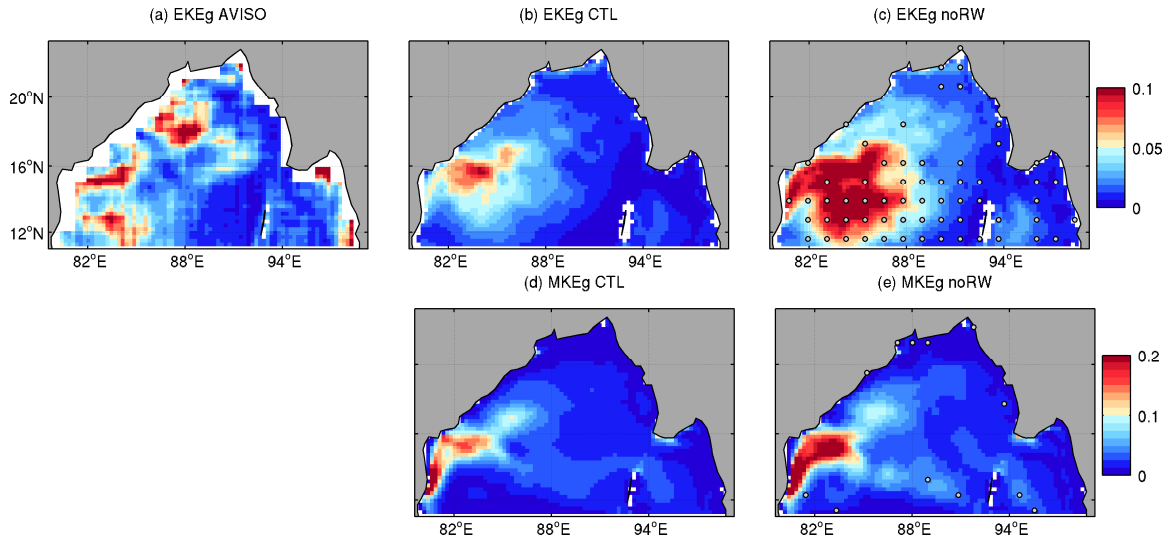

938

939 **Fig. 5.** JJAS climatologies of (top) surface geostrophic eddy kinetic energy (m^2s^{-2}) from (a) the
940 AVISO, (b) CTL and (c) noRW. Dots in (d) represent the statistical significance at 95%
941 confidence level. (d-e) as in (b-d) except for the surface mean kinetic energy (MKE, m^2s^{-2}).

942

943

944

945

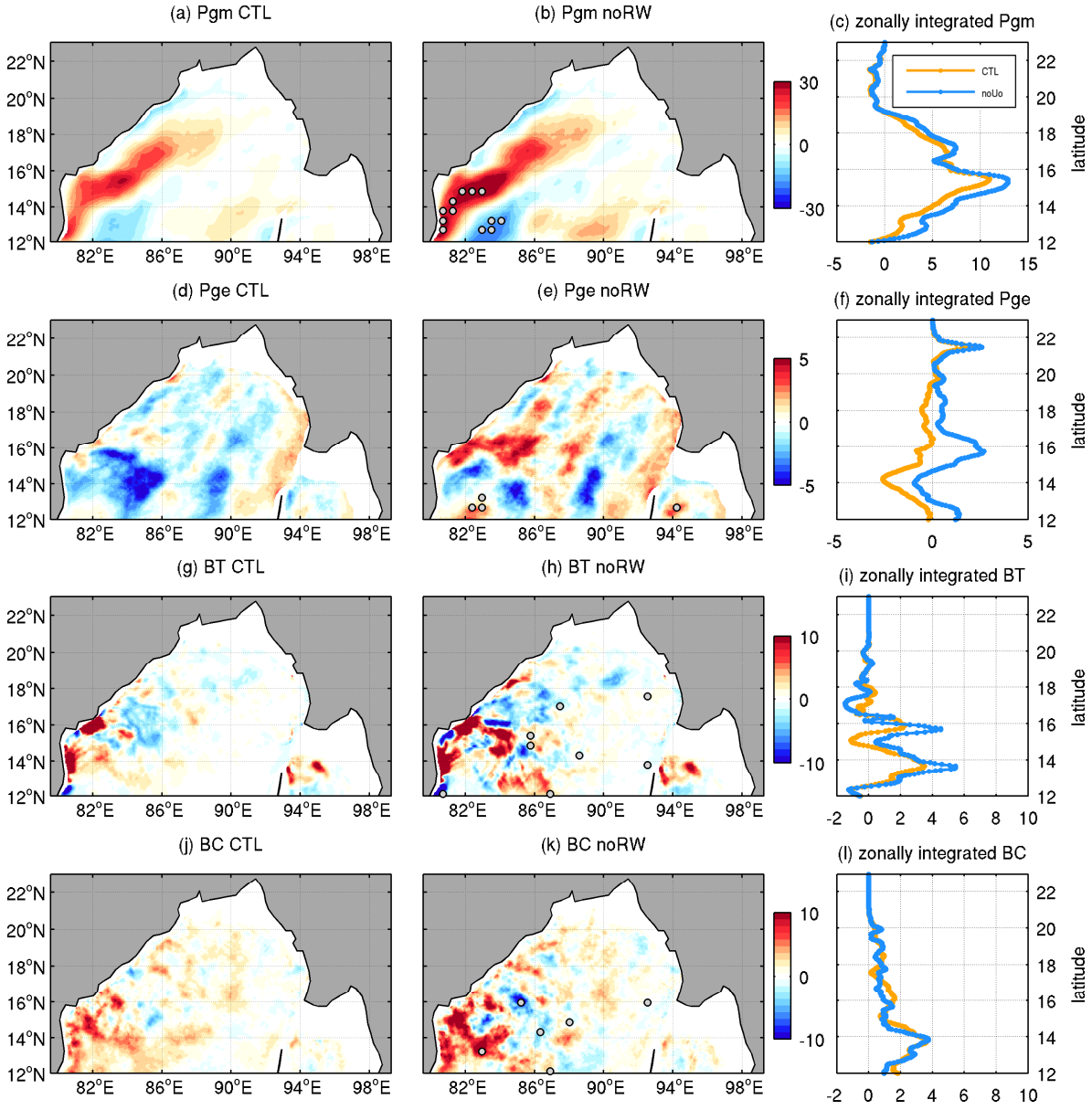

946

947 **Fig. 6.** JJAS climatologies of the energy source and depth-integrated conversion terms (10^6 m^3s^{-3}) from (left) CTL and (middle) noRW, and their zonally integrated (m^4s^{-3}) profiles as a function of latitude. Dots denote the areas of statistically significant difference between CTL and noRW at 95% confidence level.

951

952

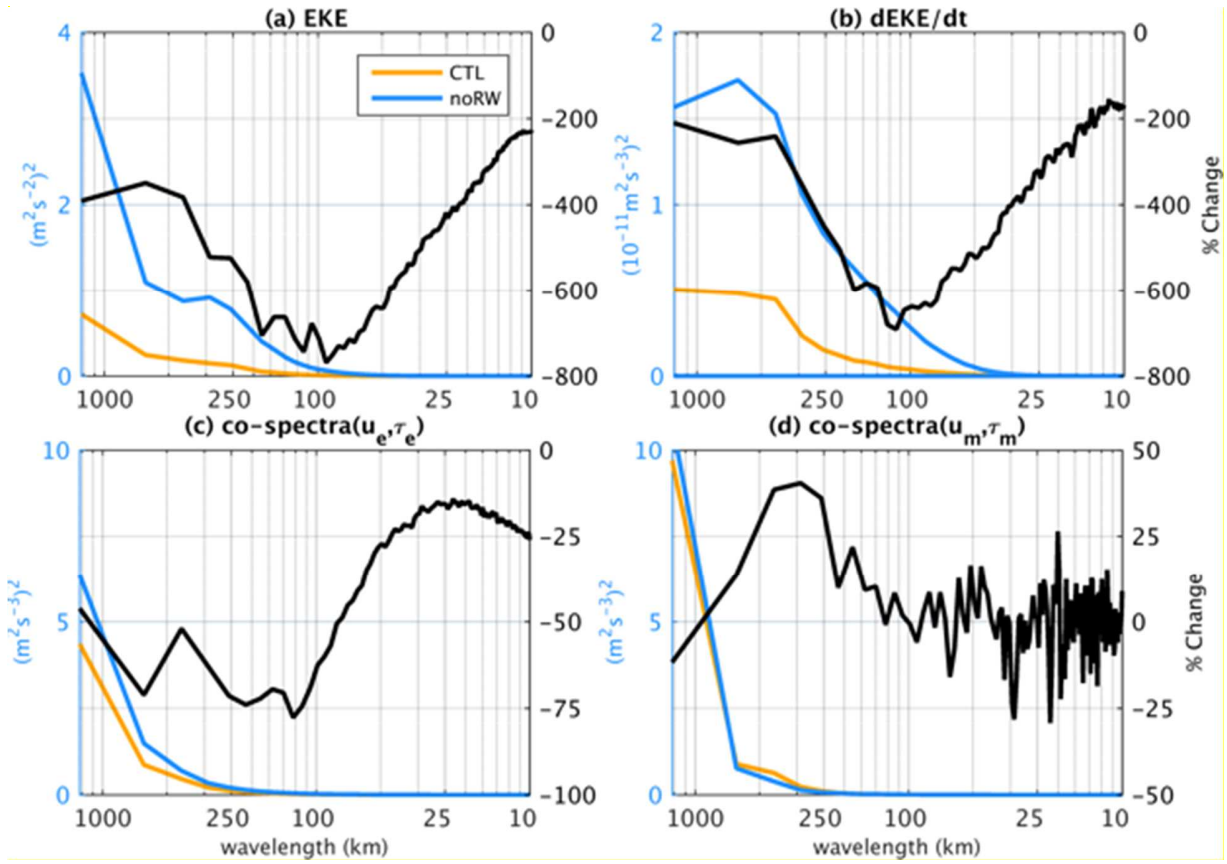

Fig. 7. The zonal wavenumber spectra of (a) EKE and (b) EKE tendency, color-coded to denote CTL (orange) and noRW (blue). (c) shows the cross-spectra of eddy current and eddy wind stress and (d) mean current and mean wind stress in the wavenumber space. Also indicated in black curve in the right axis of each panel is the percent difference in the spectra, with the negative quantities meting that the variance is reduced in CTL.

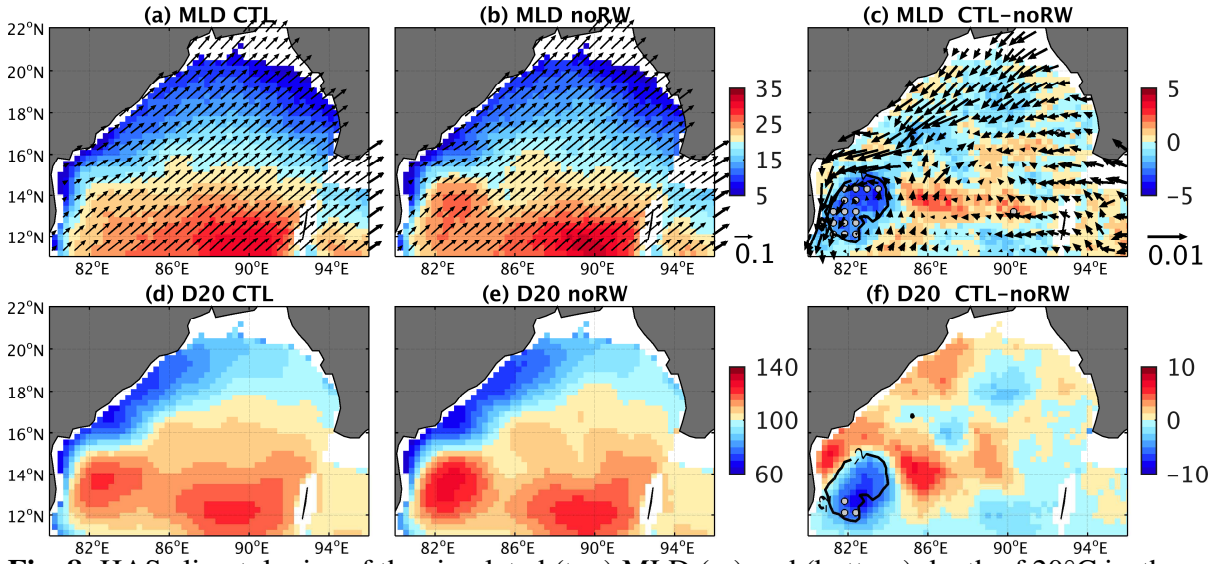

Fig. 8. JJAS climatologies of the simulated (top) MLD (m) and (bottom) depth of 20°C isotherm (D20, m) representing the depth of thermocline. The superposed vectors in the top panel indicate the wind stress (Nm^{-2}) and the difference. Dots denote the areas of statistically significant difference between CTL and noRW at 95% confidence level. The black contour in (c) and (f) denote the area of MLD reduction by 2 m, which is repeated in each of the panels in Fig. 9.

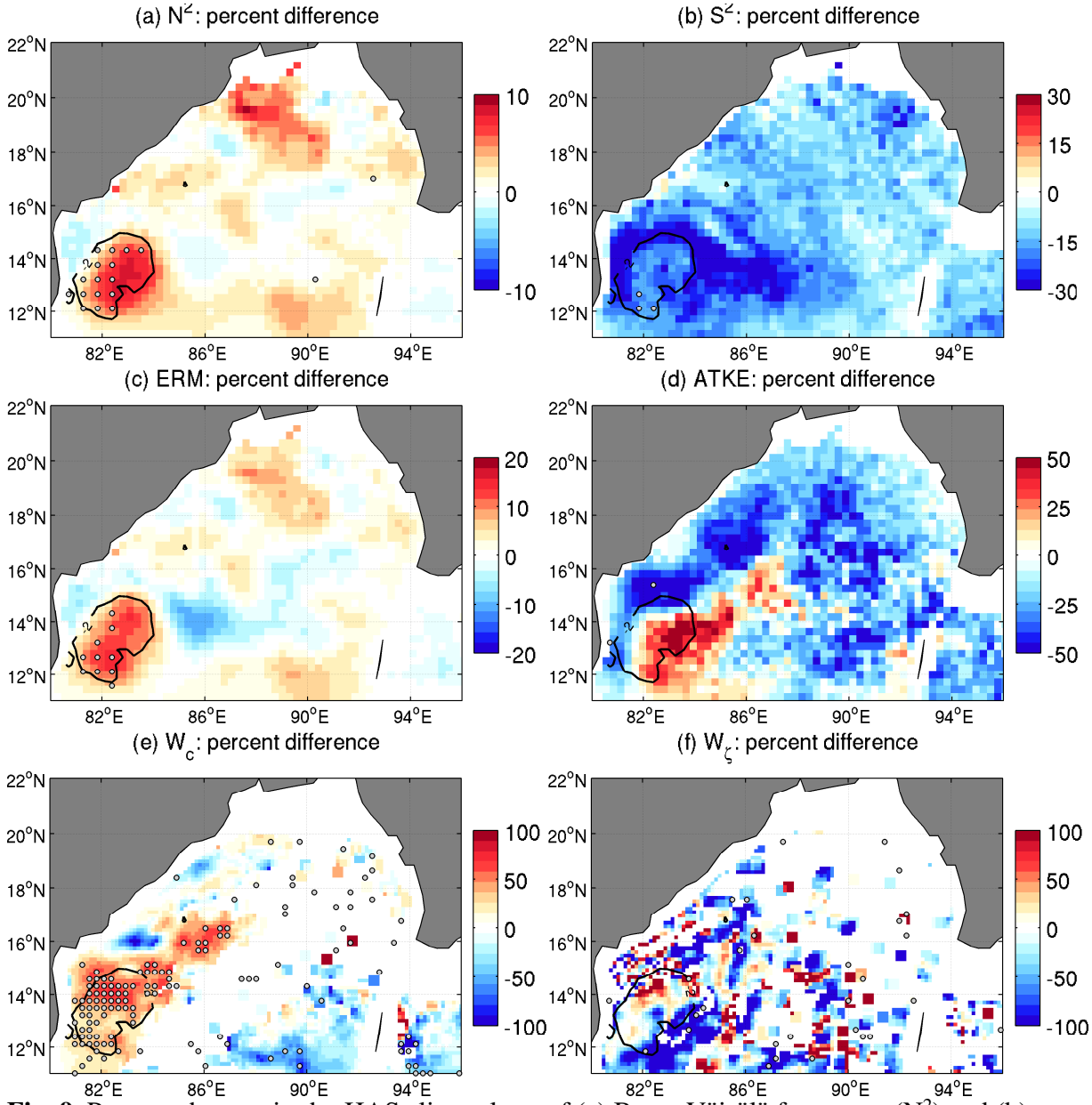

Fig. 9. Percent changes in the JJAS climatology of (a) Brunt-Väisälä frequency (N^2) and (b) vertical shear of horizontal current (S^2), both averaged over the thermocline depth (D20), (c) energy required for mixing (ERM) the D20, and (d) available turbulent kinetic energy (ATKE) from surface to the D20. (e) Percent changes in the JJAS climatology of Ekman vertical velocity due to current-wind interaction (W_c) and (f) that due horizontal vorticity gradient (W_ς). Dots represent the significance of the difference at 95% level. The black contour in (c) and (f) denote the area of MLD reduction by 2 m.

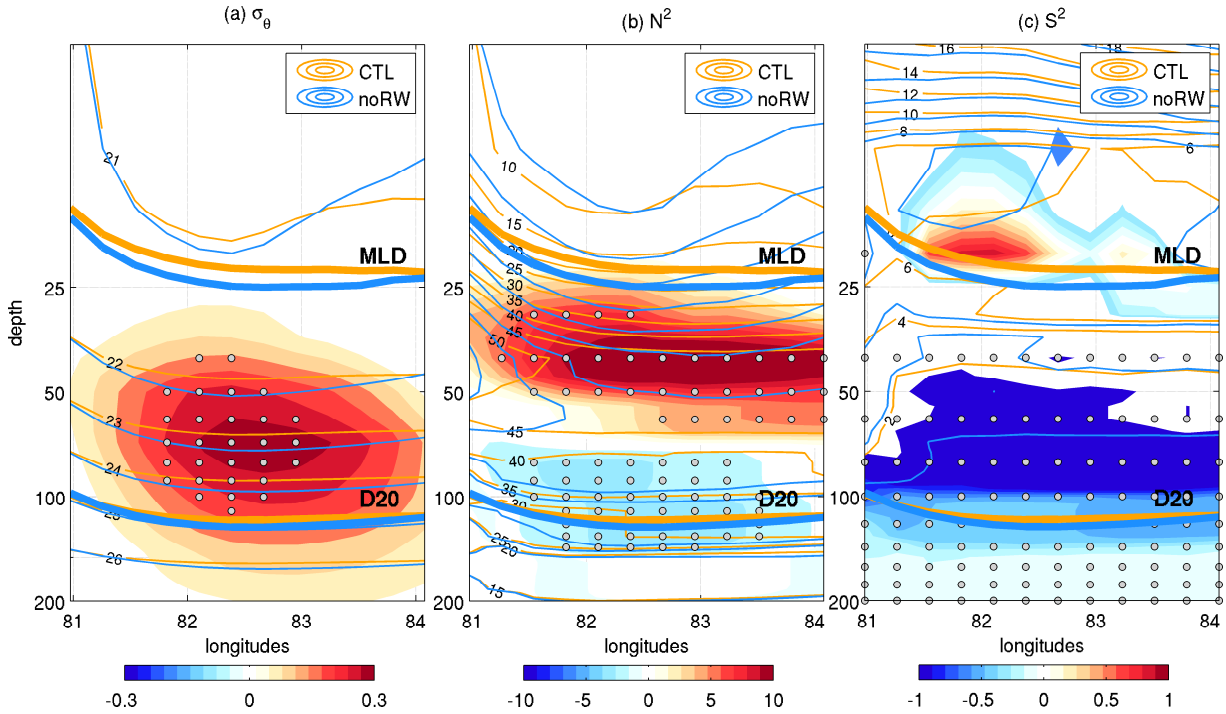

Fig. 10. Depth-longitude diagrams, averaged over 12°-15°N in the southwestern Bay of Bengal, showing (a) density (σ_θ, kgm^{-3}), (b) N^2 (10^{-5}s^{-2}), and (c) S^2 (10^{-5}s^{-2}). Note that the y-axis is in log-scale. The orange (blue) contours denote the quantities from CTL (noRW), and the color-shadings represent the difference (CTL-noRW). The thick curves at shallower (deeper) depth, repeated in each of the figures, denote the MLD (D20). Dots denote the areas of significant difference at 95% confidence level, evaluated a Monte Carlo bootstrap sampling.

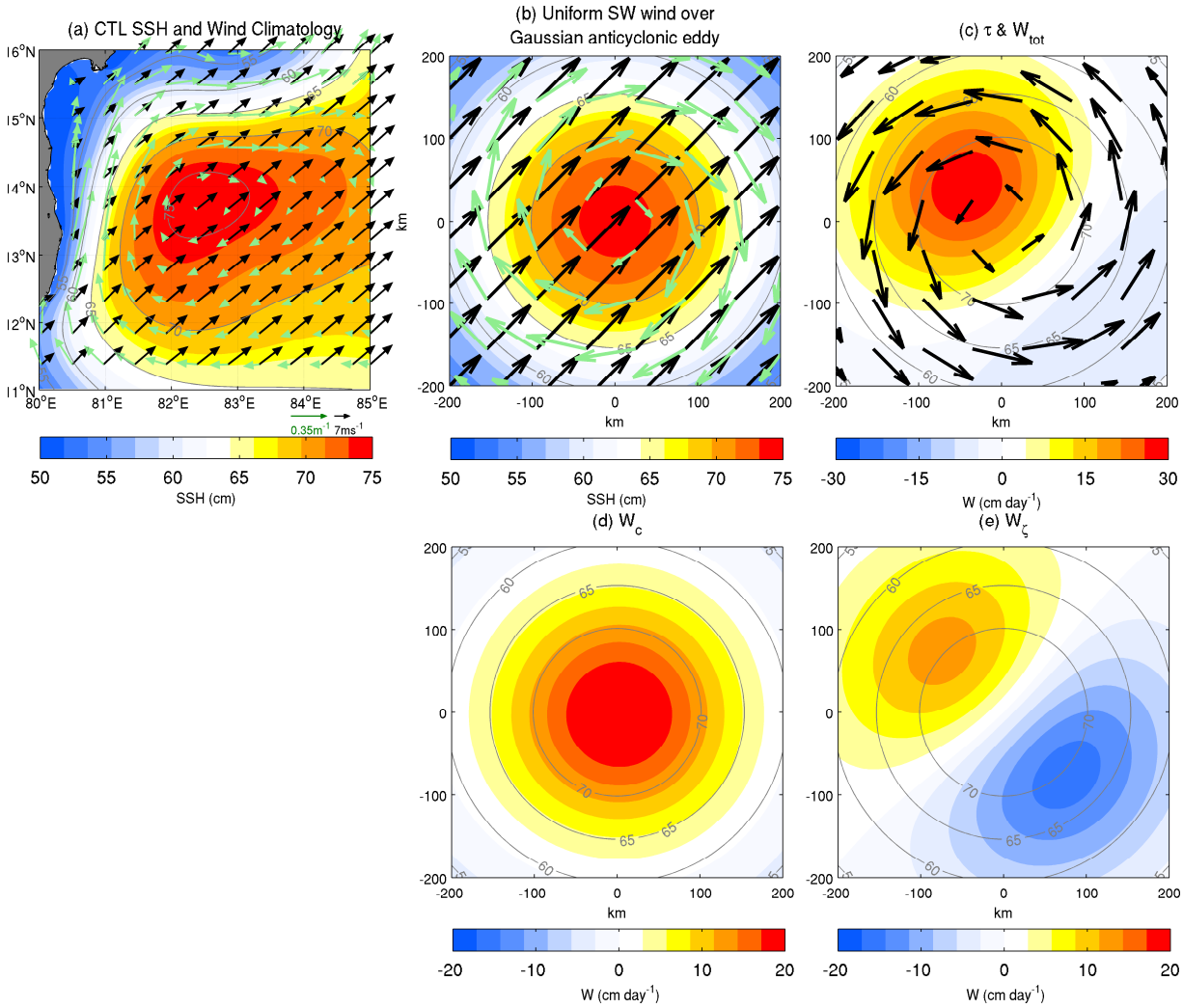

Fig. 11. (a) The simulated summertime climatologies in CTL: SSH (color shading), surface geostrophic current (green vectors), and surface wind (black vectors). (b) An idealized axis-symmetric Gaussian anticyclonic eddy interacting with the spatially uniform monsoon winds of 7 ms^{-1} (black vectors) through the surface geostrophic current (green vectors). The gray contours denote the SSHA at 5 cm interval, which is repeated in (c-e) to represent the position of the anticyclonic eddy. (c) The induced wind stress fields (black vectors) overlaid with the total Ekman vertical velocity (W_{tot}, cm day^{-1}, positive upward). (d-e) The separation of the W_{tot} into (d) that due to the relative wind effect (W_c) and (e) that due to vorticity gradient (W_ς). This figure was inspired by Chelton (2013).